

## MIT Open Access Articles

*EFFECTS OF FAST AND SLOW SOLAR WIND ON  
THE ENERGETIC NEUTRAL ATOM (ENA) SPECTRA  
MEASURED BY THE INTERSTELLAR BOUNDARY  
EXPLORER (IBEX) AT THE HELIOSPHERIC POLES*

The MIT Faculty has made this article openly available. **Please share**  
how this access benefits you. Your story matters.

**Citation:** Dayeh, M. A., D. J. McComas, F. Allegrini, B. De Majistre, M. I. Desai, H. O. Funsten, P. Janzen, et al. "EFFECTS OF FAST AND SLOW SOLAR WIND ON THE ENERGETIC NEUTRAL ATOM (ENA) SPECTRA MEASURED BY THE INTERSTELLAR BOUNDARY EXPLORER ( IBEX ) AT THE HELIOSPHERIC POLES ." The Astrophysical Journal 749, no. 1 (March 21, 2012): 50. © 2012 The American Astronomical Society

**As Published:** <http://dx.doi.org/10.1088/0004-637x/749/1/50>

**Publisher:** IOP Publishing

**Persistent URL:** <http://hdl.handle.net/1721.1/95622>

**Version:** Final published version: final published article, as it appeared in a journal, conference proceedings, or other formally published context

**Terms of Use:** Article is made available in accordance with the publisher's policy and may be subject to US copyright law. Please refer to the publisher's site for terms of use.



# EFFECTS OF FAST AND SLOW SOLAR WIND ON THE ENERGETIC NEUTRAL ATOM (ENA) SPECTRA MEASURED BY THE *INTERSTELLAR BOUNDARY EXPLORER* (IBEX) AT THE HELIOSPHERIC POLES

M. A. DAYEH<sup>1</sup>, D. J. MCCOMAS<sup>1,2</sup>, F. ALLEGRI<sup>1,2</sup>, B. DE MAJISTRE<sup>3</sup>, M. I. DESAI<sup>1,2</sup>, H. O. FUNSTEN<sup>4</sup>, P. JANZEN<sup>5</sup>, G. LIVADIOTIS<sup>1</sup>, B. M. RANDOL<sup>1,2</sup>, D. B. REISENFELD<sup>5</sup>, N. A. SCHWADRON<sup>1,6</sup>, AND R. VANDERSPEK<sup>7</sup>

<sup>1</sup> Southwest Research Institute, San Antonio, TX 78228, USA; maldayah@swri.edu

<sup>2</sup> Department of Physics and Astronomy, University of Texas at San Antonio, San Antonio, TX 78249, USA

<sup>3</sup> Applied Physics Laboratory, Johns Hopkins University, Laurel, MD 20723, USA

<sup>4</sup> Los Alamos National Laboratory, Los Alamos, NM 87545, USA

<sup>5</sup> University of Montana, Missoula, MT 59812, USA

<sup>6</sup> Space Science Center, University of New Hampshire, Durham, NH 03824, USA

<sup>7</sup> Center for Space Research, Massachusetts Institute of Technology, Cambridge, MA 02139, USA

Received 2011 December 16; accepted 2012 January 31; published 2012 March 21

## ABSTRACT

We study the energy dependence of  $\sim 0.5$ – $6$  keV energetic neutral atom (ENA) spectra in the southern heliospheric polar region obtained during five six-month sky maps measured by *IBEX*-Hi. We calculate the spectral slopes in the south pole in four different energy bands, namely,  $\sim 0.7$ – $1.1$  keV,  $\sim 1.1$ – $1.7$  keV,  $\sim 1.7$ – $2.7$  keV, and  $\sim 2.7$ – $4.3$  keV. We show (1) a persistent flattening of the ENA spectrum between  $\sim 1$  and  $2$  keV, (2) significantly different modes (2.31, 1.58, 0.97, and 1.44) for the distributions of the slopes in the four different energy bands, and (3) a general decrease with increasing energy in the widths (FWHM) and mode fluctuations (their spread) of the slope distributions. We also compare the averaged ENA spectra measured at the south pole and at mid-latitudes. We conclude that the flattening between  $\sim 1$  and  $2$  keV in the polar spectrum (spectral break) is produced by an enhancement of ENAs created by charge exchange between interstellar neutrals and pick-up ions in the fast solar wind.

**Key words:** plasmas – ISM: kinematics and dynamics – solar wind – Sun: heliosphere

## 1. INTRODUCTION

The heliosphere is an asymmetric bubble-like cocoon inflated in the interstellar medium by the continuous outflow of the solar wind (SW) from the Sun. The boundary of the heliosphere (the heliopause) is where the SW pressure, magnetic and thermal, balances the pressure of the weakly ionized plasma of the interstellar medium. When it approaches the heliopause, the supersonic and super-Alfvénic SW slows down in an abrupt shock, the heliospheric termination shock (HTS). As the interstellar neutrals drift through the heliosphere, some of them become ionized through charge exchange or photoionization, and are then picked up by the flow, becoming pick-up ions (PUIs), gaining energy from the motional electric field produced by the SW's embedded interplanetary magnetic field. By the time the SW reaches the HTS, the SW is slightly decelerated and significantly loaded with PUIs, a population which is more energetic and hotter (wider velocity distribution) and thus contains a significant fraction of the total pressure.

In the inner heliosheath (IHS) between the HTS and heliopause, part of the recently shocked (slowed down and heated) SW and PUIs charge exchange with the cold interstellar neutrals and are converted to energetic neutral atoms (ENAs). The rest eventually get deflected along the flow streamlines toward the heliospheric tail. Being neutral, ENAs propagate through the heliosphere unaffected by electric or magnetic fields. Some of them reach the Earth and can thus be exploited to trace them back to their source region. This provides a remote sensing capability to understand the properties and interactions of different energetic ion populations beyond the HTS. The dominant particle populations downstream of the HTS are (1) SW, observed to be  $\sim 2$  times slower and  $\sim 10$  times hotter than the upstream SW as measured by *Voyager*-2 (Richardson et al. 2008; Richardson 2008), and possibly  $\sim 10$ – $100$  times across the sky as remotely

inferred by *IBEX* (Livadiotis et al. 2011), (2) heliospheric PUIs, a more energetic and hotter population entrained in the upstream SW and carried across the HTS, (3) local PUIs, which are created in the IHS and whose role becomes more significant away from the HTS, and (4) a suprathermal tail of power-law index  $-1.5$  in differential energy observed at significantly higher energies (e.g., Gloeckler et al. 2009). Interactions between these different populations in the downstream region are complex and difficult to predict. Turbulence in the IHS (Shevryev et al. 2003) and the highly variable plasma properties over short timescales observed by *Voyager* (Richardson 2011) could play a role in modifying the IHS distributions constantly. Moreover, it is shown that PUIs and SW protons passing through the HTS behave differently and their thermal signatures change substantially throughout the IHS (e.g., Fahr & Chalov 2008; Chalov & Fahr 2011).

The *Interstellar Boundary Explorer* (*IBEX*) mission (McComas et al. 2009a) continues to measure heliospheric ENAs from all directions in the sky, providing unprecedented insights into the physical processes that take place at the edge of our solar system and beyond (see a recent review by McComas et al. 2011b). *IBEX* is equipped with two neutral atom cameras, *IBEX*-Lo (Fuselier et al. 2009) and *IBEX*-Hi (Funsten et al. 2009), capable of measuring ENAs with energies  $\sim 0.01$ – $2$  keV and  $\sim 0.3$ – $6$  keV, respectively. Both sensors observed an unpredicted ribbon-like structure in the sky superimposed over globally distributed ENA flux, which is a factor of  $\sim 2$ – $3$  lower in intensity than the ribbon (McComas et al. 2009b; Schwadron et al. 2011). Energy spectra across different structures and regions of the sky are found to have distinct shapes (Dayeh et al. 2011, and references therein), sometimes steepening with increasing energies (slope increases; e.g., ribbon), flattening (slope decreases; e.g., poles), or following a single power law across all energies (e.g., globally distributed fluxes).

Of specific interest are the ENA spectra at the polar regions, which have a unique persistent break at which the spectra flatten significantly between  $\sim 1$  and  $\sim 2$  keV (ankle break). McComas et al. (2009b) suggested that this ankle break might be attributed to the fast SW, which generates and entrains higher-energy PUIs than near the ecliptic. Measurements from *Ulysses*/SWOOPS (Bame et al. 1992) showed that the fast SW speed at high latitudes is roughly double the speed of the slow SW near the equator during solar minimum (McComas et al. 2000). Dayeh et al. (2011) studied the ENA spectral behavior across a full latitude region of the sky (north pole–tail–south pole) and found that it correlates well with bulk SW speed variations measured by *Ulysses*/SWOOPS during its fast latitudinal scan around the Sun in 2007, with clear latitudinal boundaries at  $\sim 36^\circ$  (north) and  $\sim 40^\circ$  (south).

Recent studies of the polar regions have also shown that they are dynamic regions, exhibiting temporal variations at long ( $\sim 6$  months; McComas et al. 2010) and short ( $\sim$  weeks; Reisenfeld et al. 2012) timescales. Reisenfeld et al. (2012) examined the short-time temporal variations in polar fluxes over a period of two years and found that variations in ENA fluxes are energy dependent, with a general trend of declining fluxes that are well correlated with the decrease of SW dynamic pressure observed at 1 AU. Finally, Allegrini et al. (2012) applied a time-dispersion correction to the ENA spectra at the polar regions assuming an HS thickness of  $\sim 55$  AU and found that after accounting for the delay in travel times of ENAs at each energy, the resulting spectra at the poles are generally flatter.

In this paper, we study the energy dependence of  $\sim 0.5$ – $6$  keV ENA spectra in the southern heliospheric polar region obtained during five six-month sky maps. We show that the ENA polar spectrum is constructed from PUI-generated ENA fluxes in both slow and fast SW populations.

## 2. OBSERVATIONS

Instruments on board the *IBEX* spacecraft, launched in 2008 October, are designed to detect ENAs generated from the interaction regions of the heliosphere and interstellar medium. *IBEX* is an Earth-orbiting, Sun-oriented, spinning spacecraft (4 RPM) that images the heliosphere in orbital swaths, utilizing Earth's and its own orbital motions to construct full sky maps every six months (McComas et al. 2009a). Due to the nature of this motion, *IBEX* views both poles almost continuously (four times every minute in each sensor), thus providing better statistics and temporal resolution for these regions.

In this paper, we study the energy dependence of fluxes obtained by *IBEX*-Hi in four different energy ranges between  $\sim 0.5$  keV and  $\sim 6.0$  keV from the southern polar region, at ecliptic latitudes of  $72^\circ$ – $90^\circ$  and at all ecliptic longitudes. These data were taken between 2008 December and 2011 May and derive from orbits 11 through 125, just prior to the new *IBEX* orbit maneuver in 2011 June (McComas et al. 2011a). We do not consider the northern pole here because of its proximity to the ribbon at high latitudes, which appears to overlap a significant fraction of the northern pole, especially at high energies where it appears to broaden and dissipate at all latitudes (Schwadron et al. 2011). The dataset used in this study accounts for a small decrease in instrument background associated with the continuous decrease of background galactic cosmic rays which have dropped by  $\sim 30\%$  from their peak rate in 2010 January (Reisenfeld et al. 2012). Corrections coming from the

modification of the ENA energy due to the action of radiation pressure and the gravitational deflection of ENAs toward the Sun (see Bzowski 2008) are not accounted for, as these effects are negligible for ENAs above a few hundred eV. Moreover, the fluxes presented here have not been corrected for the ENA loss effects as they propagate from their source to 1 AU, thus the ENA spectra presented here do not necessarily reflect the spectra close to the HTS. McComas et al. (2010) showed that differences from this effect between observations taken in the first and second six months of *IBEX* observations were small ( $\sim 10\%$ ). Another aspect of data correction comes from the travel time of ENAs at different energies, which travel at different speeds and thus arrive at *IBEX* at different times. This time-dispersion effect is examined in Allegrini et al. (2012) and was found to slightly flatten the spectral shapes at 1 AU. Finally, an additional correction to the data comes from the finite speed of the proper motion of the *IBEX* spacecraft (detectors) with respect to the Sun, i.e., the Compton–Getting (C-G) effect. This effect is at maximum along the flow velocity vector and decreases as the cosine with latitude until it vanishes at the poles. However, this correction does not exceed  $\sim 15\%$  at the energies being studied here ( $>0.5$  keV). We correct for this at the mid-latitudinal range examined later but not at the  $\sim 18^\circ$  polar cap region, where the uncertainty due to this effect does not exceed a maximum of  $\sim 5\%$  at  $72^\circ$  (latitude) and  $\sim 0.7$  keV.

Using fluxes measured at *IBEX*-Hi energy channels centered at [in keV]  $\sim 0.71$  (ESA2),  $\sim 1.11$  (ESA3),  $\sim 1.74$  (ESA4),  $\sim 2.73$  (ESA5), and  $\sim 4.29$  (ESA6), we study the energy dependence of ENA spectra in each pixel for the four adjacent energy band pairs: ESA2–3, ESA3–4, ESA4–5, and ESA5–6. To minimize the statistical uncertainties due to low exposure times, we exclude pixels with exposure times less than 25% of the maximum exposure time for each energy channel. In addition, pixels with fluxes associated with  $1\sigma$  errors equal to or greater than the fluxes themselves are also excluded. Both criteria result in the removal of noisy orbits in each map at different energies. Figure 1(a) shows the first six-month ENA skymap at  $\sim 1.74$  keV in the spacecraft frame with the prominent ribbon feature discovered by *IBEX* (McComas et al. 2009b). Figure 1(b) shows the same map after excluding pixels with high relative uncertainties and low relative exposure times. Red boxes mark the pixels used in this study. We note that excluded pixels (appearing in black in Figure 1) differ for each energy channel and for each six-month map.

The regions identified in this figure were analyzed for all five six-month maps. Figure 2 shows the exposure-weighted polar spectra selected from each of the five ENA maps. Although fluxes at some energies appear to fluctuate up and down, the general trend is consistent with a flux decrease at all energies between maps 1 and 5, but at different rates. We note that the lowest energy channel, ESA2, is the most susceptible channel to residual SW contamination, thus should be interpreted with care. In addition, without correcting for survival probabilities of ENAs in the heliosphere, the apparent changes over time are not necessarily temporal variations in the source ENAs. On the other hand, the persistent “ankle” break (flattening of spectra) at ESA4, reported earlier in the first two six-month maps at both poles (Dayeh et al. 2011), appears in the polar regions of all five maps. The fact that such behavior exists in all maps demonstrates that this is a true physical effect and not the result of statistical fluctuations.

We calculated the spectral slope between each pair of adjacent energy channels (energy bands) for each pixel in the sky for each

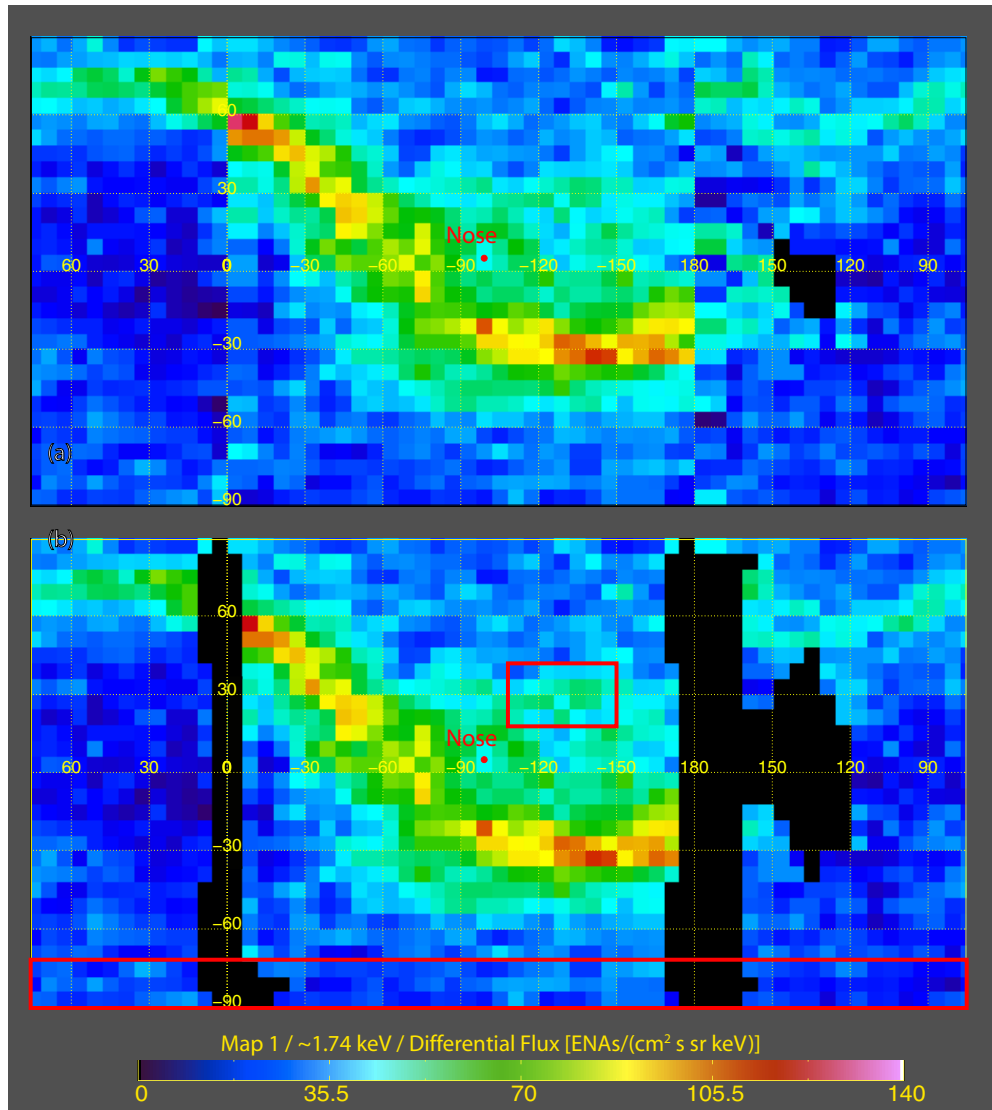


**Figure 1.** (a) First *IBEX* ENA sky map (orbits 11 through 33) at  $\sim 1.74$  keV in the spacecraft frame. (b) Black areas indicate pixels with low exposure times and are excluded from this analysis (see the text for details). Red boxes mark the pixels used in this study at this energy channel and for this sky map.

map as

$$\text{Slope} = \frac{\text{Ln} \left( \frac{j_i}{j_{i+1}} \right)}{\text{Ln} \left( \frac{E_i}{E_{i+1}} \right)}, \quad (1)$$

where  $j_i$  is the flux measured at energy step  $E_i$ . The uncertainty is then given by

$$\text{Uncertainty} = \frac{1}{\text{Ln} \left( \frac{E_i}{E_{i+1}} \right)} \times \sqrt{\left( \frac{\sigma_{j_i}}{j_i} \right)^2 + \left( \frac{\sigma_{j_{i+1}}}{j_{i+1}} \right)^2}. \quad (2)$$

Figure 3 shows the histograms of slopes of the south pole pixels calculated at four different energy bands integrated over all five maps. The best fits to the data show that slopes are normally distributed (smooth lines). This figure reveals some interesting features about the energy dependence of the polar spectra: (1) slope distributions are characterized by modes that are unique at every energy band; (2) as energy increases, spectra flatten through the first three energy bands, then steepen at the fourth energy band; (3) the distribution of slopes for ESA5–6

(shown in blue) is significantly, by a factor of two, narrower than the other three bands, which all have about the same width.

We plot in Figure 4 the modes versus the full width at half-maximum (FWHM) of the fitted slope distributions from all five individual maps. Shaded regions surround points that belong to the same energy band and black-filled symbols are the mean values from all maps at each energy band. This figure shows that (1) the behavior of the slopes described in Figure 3 occurs consistently at the poles in each of the five different maps and (2) spread of the points around the mode decreases with increasing energy. The clearest contrast in spread is between the lowest and the highest energy bands. At ESA5–6, slope distribution modes from all maps are strikingly similar, with four map modes very close to 1.44, while the lowest energy band (ESA2–3) shows the largest variability with modes varying between 2 and 2.6. Values shown in this figure are listed in Table 1.

### 3. DISCUSSION

*IBEX* ENA spectra provide information about the progenitor ion spectra resulting from the superposition and/or interactions

**Table 1**  
Properties of Slope Distributions in the Polar Regions (lat.  $72^\circ$ – $90^\circ$ ) calculated at Four Different Energy Bands in Five ENA Sky Maps

Energy Band	Map 1		Map 2		Map 3		Map 4		Map 5	
	Mode	FWHM	Mode	FWHM	Mode	FWHM	Mode	FWHM	Mode	FWHM
ESA2–ESA3	$2.07 \pm 0.05$	$1.19 \pm 0.11$	$2.13 \pm 0.07$	$1.55 \pm 0.18$	$2.53 \pm 0.04$	$1.38 \pm 0.08$	$2.2 \pm 0.1$	$2.64 \pm 0.24$	$2.41 \pm 0.06$	$1.2 \pm 0.14$
ESA3–ESA4	$1.75 \pm 0.05$	$1.29 \pm 0.11$	$1.43 \pm 0.1$	$1.51 \pm 0.24$	$1.63 \pm 0.06$	$1.56 \pm 0.15$	$1.19 \pm 0.11$	$2.04 \pm 0.26$	$1.44 \pm 0.06$	$1.1 \pm 0.15$
ESA4–ESA5	$1.08 \pm 0.05$	$1.22 \pm 0.12$	$1.09 \pm 0.09$	$1.53 \pm 0.24$	$0.81 \pm 0.06$	$1.33 \pm 0.14$	$0.93 \pm 0.08$	$1.56 \pm 0.02$	$0.87 \pm 0.06$	$1.03 \pm 0.14$
ESA5–ESA6	$1.46 \pm 0.02$	$0.62 \pm 0.06$	$1.5 \pm 0.05$	$0.76 \pm 0.12$	$1.44 \pm 0.02$	$0.69 \pm 0.05$	$1.43 \pm 0.03$	$0.8 \pm 0.07$	$1.30 \pm 0.03$	$0.46 \pm 0.07$

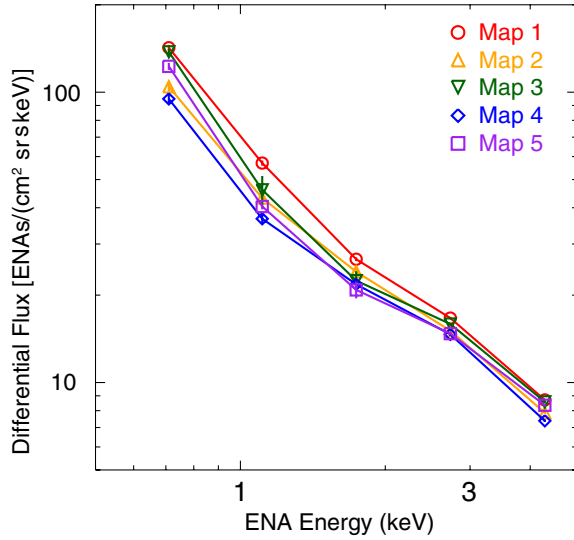


**Figure 2.** Exposure-weighted energy spectra of the southern polar region (latitude  $72^\circ$ – $90^\circ$ ) in five six-month ENA sky maps at five energy channels centered at (in keV)  $\sim 0.71$  (ESA2),  $\sim 1.11$  (ESA3),  $\sim 1.74$  (ESA4),  $\sim 2.73$  (ESA5), and  $\sim 4.29$  (ESA6).

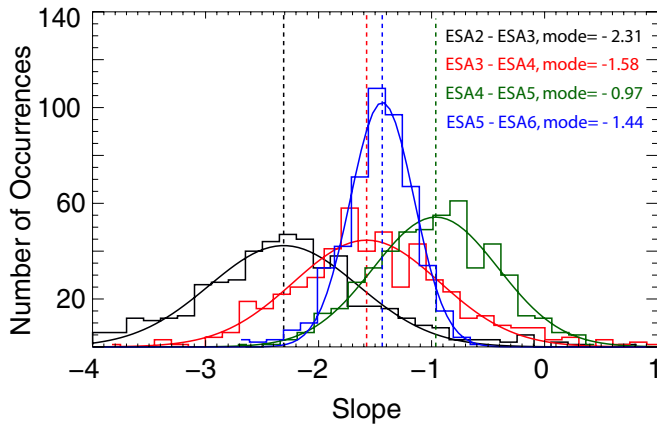


**Figure 3.** Histograms of slopes calculated at four different energy bands (ESA2–3, ESA3–4, ESA4–5, ESA5–6) in the southern polar region pixels accumulated from five sky maps. Smooth lines represent normal fits and dashed vertical lines mark the modes of these fits.

of these different populations in the IHS, integrated over the line of sight through the IHS in different directions of the sky. Since the travel times of ENAs at different energies are not the same and probably longer than the timescale of variations in the heliosheath, different parts of *IBEX*'s ENA spectrum likely refer to different IHS populations at different energies, and the observed ENA spectrum at 1 AU serves as an indicator of the physical trends in the IHS.

Figure 5(a) shows a schematic of the heliospheric boundaries and illustrates the streamlines for the fast and slow SW flows in

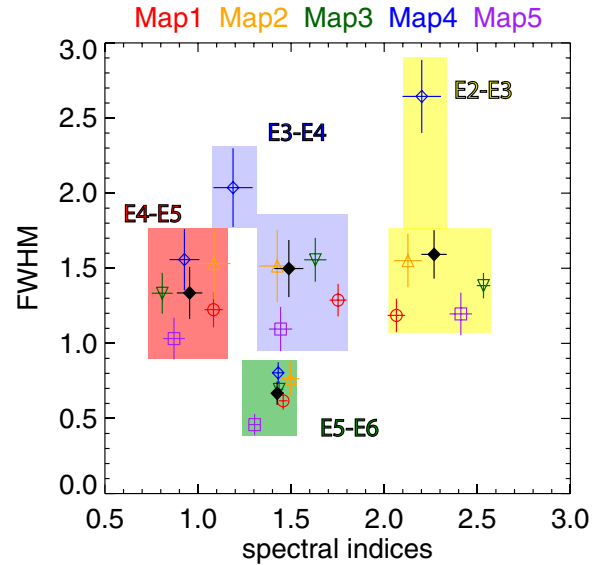


**Figure 4.** Widths (FWHM) of the slope distributions determined at four different energy bands plotted against the modes of these distributions. Shaded regions mark the spread at each energy band. Color-coded open symbols correspond to different maps. Black filled symbols represent the mean values at the same energies for all maps.

the IHS. The slow SW streamlines are deflected from the nose toward the tail over the poles, enabling it to exist in all viewing directions in the sky. The latitudinal extent of the fast SW flows depends on solar activity and the configuration of coronal holes. At the poles, *IBEX* should observe ENAs generated by charge exchange with ion populations in both the fast (red flow lines) and slow (blue flow lines) SW. In contrast, at the nose and mid-latitudes, *IBEX* ENAs are generated by ion populations existing primarily in the slow SW.

Figure 5(b) shows the 2.5-year-averaged *IBEX* polar spectrum (red), compared with the average spectrum at mid-latitudes (blue). While the mid-latitude ( $18^\circ$ – $42^\circ$ ) ENA spectrum behaves approximately as a power law, the polar spectrum clearly shows a significant deviation (intensity enhancement) away from a power law at  $\sim 1.74$  keV (ESA4), creating a characteristic ankle break at the poles. The spectra in both cases behave similarly at lower energies.

In order for *IBEX* to detect ENAs produced by any ion, the ion's velocity vector must be directed toward *IBEX*. Livadiotis et al. (2012) used a geometrical projection approach on the downstream distributions reflected in the direction of *IBEX* and found that for typical values for the compression ratio and upstream flow speeds up to  $\sim 700$  km s $^{-1}$ , *IBEX*-Hi should observe PUI-generated ENAs in all of its energy channels, while for flow speeds up to  $\sim 350$  km s $^{-1}$ , PUI-generated ENAs downstream would be observed up to ESA3 ( $\sim 1.11$  keV) of

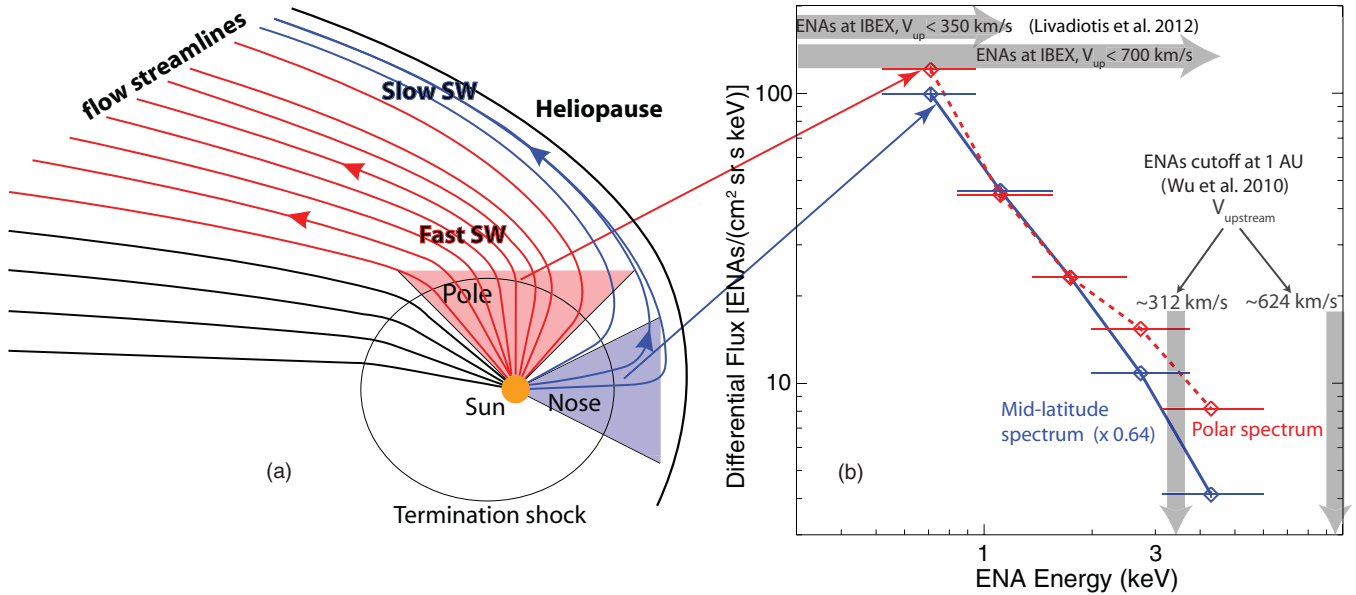


**Figure 5.** (a) Schematic illustration of how an observer looking along the nose/mid-latitudes of the heliosphere sees only the downstream slow solar wind component, while along the polar region the observer sees both fast solar wind and deflected slow solar wind downstream. Streamlines shown here are based on the Izmodenov & Alexashov (2003) model. (b) Averaged ENA spectra at the southern pole (dashed red) and mid-latitude (solid blue) regions in five maps normalized at  $\sim 1.74$  keV for comparison purposes. Horizontal arrows indicate the expected range of ENAs that *IBEX* would observe due to the ENA velocity vector orientations in the IHS (Livadiotis et al. 2012), vertical arrows mark the approximate cutoffs of ENA fluxes at 1 AU as derived from hybrid simulations of the HTS at two upstream SW speeds (Wu et al. 2010).

*IBEX*-Hi. These ranges are indicated by the horizontal arrows in Figure 5(b).

Moreover, using hybrid simulations of the HTS, Wu et al. (2010) constructed downstream ion velocity distributions for upstream SW speeds at three different Alfvén Mach numbers,  $M_A \sim 4, 8$ , and  $16$ , which correspond to bulk velocities of  $\sim 156, 312$ , and  $624$  km s $^{-1}$ , respectively. In each case, they estimated the contributions of PUI-generated ENA fluxes and spectra at 1 AU and found that faster SW flows lead to increased fluxes of ions in the suprathermal tails. These simulations showed that for  $M_A \sim 8$ , the ENA flux cutoff is about  $\sim 4$  keV, while for  $M_A \sim 16$ , PUI-generated ENAs observed at 1 AU extend up to  $\sim 10$  keV, i.e., well beyond the upper limit of the *IBEX*-Hi energy range; approximate locations of these cutoff values are indicated by the vertical arrows in Figure 5(b). The superposition of ENA fluxes from slow and fast downstream distributions from Wu et al. would create an ankle break in the polar spectrum at  $\sim 3$  keV, slightly higher than the break location observed by *IBEX* at the polar regions. However, after considering the projection effect for ENAs traveling toward *IBEX* from different directions discussed by Livadiotis et al. (2012), the spectral break would shift toward lower energies, moving it closer to the break location observed in the polar spectra.

Our interpretation of the data is that at low latitudes, heated PUIs from the slow SW are the only ones present, whereas at the poles the overall ENA spectrum is generated from a superposition of the slow and fast PUIs. We attribute the ankle break observed in the polar spectra to the dominant contribution of ENAs generated from PUIs in the fast SW, while the lower energy portion of the spectrum is mainly produced by the slow PUI component, which exists at all latitudes.

We note that the downstream distributions are extremely complex to predict and thus quantifying the relative contributions of each population to the *IBEX* ENA spectrum requires a rigorous fitting using a global model that accounts for numerous assumptions, and this is beyond the scope of this paper. For instance,

the compression ratio is expected to vary substantially along the HTS. Therefore, the detailed distribution function in the downstream region is expected to be a function of the upstream SW speeds, distance from the HTS, the position of the HTS, and the fluxes of both SW and PUIs (e.g., Fahr & Chalov 2008; Chalov & Fahr 2011; Wu et al. 2010; Livadiotis et al. 2012).

The large differences in the widths of the slope distributions in the low (ESA 2–3) and high energy bands (ESA 5–6), as shown in Figure 3, could possibly be direct signatures of the inherent variations in the properties of slow and fast SW. For instance, the slow SW was found to be more variable than the fast SW (see, e.g., McComas et al. 2000). Such variations are likely to be transmitted across the HTS and could affect the lower energy portions of the resulting ENA spectrum. Moreover, the steepening of the ENA spectrum above  $\sim 2.74$  keV which is consistent in all maps over the 2.5 year interval (see Table 1), along with the focused mode spread around  $\sim 1.44$ , could also be due to ENAs generated by a suprathermal ion tail in the IHS.

#### 4. CONCLUSION

Using data from the first five sky maps measured by *IBEX*-Hi, we studied the energy dependence of the  $\sim 0.5$ – $6$  keV ENA spectra in the southern polar regions in four separate energy bands, namely ESA2–3, ESA3–4, ESA4–5, and ESA5–6. We find the following: (1) polar spectra in all sky maps exhibit a significant and persistent flattening at energies between  $\sim 1$  and  $\sim 2$  keV (see Figure 2); (2) slope distributions in these four energy bands are characterized by significantly different modes of 2.31, 1.58, 0.97, and 1.44, respectively (Figure 3); (3) the FWHM of the slope distributions decreases with increasing energy (see Figure 3 and Table 1); and (4) mode fluctuations (spread) also decrease with increasing energy (Figure 4, Table 1).

We have studied the energy dependence of polar ENA spectra over a period of two-and-a-half years and found that the

persistent spectral ankle break observed in the polar spectra between  $\sim 1$  and 2 keV is due to ENAs generated by PUIs in the fast SW in the IHS. Detailed theoretical modeling coupled with comparisons of such observations will further enhance our understanding of the different populations in the heliosheath and their relative contributions to the observed ENA spectrum at 1 AU.

We thank all the outstanding men and women who have made *IBEX* such a successful mission. Work at LANL was carried out under the auspices of the U.S. Department of Energy. This research was carried out as a part of the NASA *IBEX* mission. M.A.D. thanks Haifa Ismail for helping with Figure 5.

## REFERENCES

- Allegrini, F., Bzowski, M., Dayeh, M. A., et al. 2012, *ApJL*, submitted
- Bame, S. J., McComas, D. J., Barraclough, B. L., et al. 1992, *A&AS*, **92**, 237
- Bzowski, M. 2008, *ApJ*, **488**, 1057
- Chalov, S. V., & Fahr, H. J. 2011, *Adv. Space Res.*, **47**, 9
- Dayeh, M. A., McComas, D. J., Livadiotis, G., et al. 2011, *ApJ*, **734**, 29
- Fahr, H. J., & Chalov, S. V. 2008, *A&A*, **490**, L35
- Funsten, H. O., Allegrini, F., Bochsler, P., et al. 2009, *Space Sci. Rev.*, **146**, 75
- Fuselier, S. A., Bochsler, P., Chornay, D., et al. 2009, *Space Sci. Rev.*, **146**, 117
- Gloeckler, G., Fisk, L. A., Geiss, J., et al. 2009, *Space Sci. Rev.*, **143**, 163
- Izmodenov, V., & Alexashov, D. 2003, *Astron. Lett.*, **29**, 58
- Livadiotis, G., McComas, D. J., Dayeh, M. A., Funsten, H. O., & Schwadron, N. A. 2011, *ApJ*, **734**, 1
- Livadiotis, G., McComas, D. J., Randol, M. B., et al. 2012, *ApJ*, in press
- McComas, D. J., Allegrini, F., Bochsler, P., et al. 2009a, *Space Sci. Rev.*, **146**, 11
- McComas, D. J., Allegrini, F., Bochsler, P., et al. 2009b, *Science*, **326**, 959
- McComas, D. J., Barraclough, B. L., Funsten, H. O., et al. 2000, *J. Geophys. Res.*, **105**, 10419
- McComas, D. J., Bzowski, M., Frisch, P., et al. 2010, *J. Geophys. Res.*, **115**, 09113
- McComas, D. J., Carrico, J. P., Hautamaki, B., et al. 2011a, *Space Weather*, **9**, S11002
- McComas, D. J., Funsten, H. O., Fuselier, S. A., Lewis, W. S., Möbius, E., & Schwadron, N. A. 2011b, *Geophys. Res. Lett.*, **38**, L18101
- Reisenfeld, D. B., Allegrini, F., Bzowski, M., et al. 2012, *ApJ*, **747**, 110
- Richardson, J. D. 2008, *Geophys. Res. Lett.*, **35**, L23104
- Richardson, J. D. 2011, *ApJ*, **740**, 113
- Richardson, J. D., Funsten, H. O., Fuselier, S. A., et al. 2008, *Nature*, **464**, 63
- Schwadron, N. A., Allegrini, F., Bzowski, M., et al. 2011, *ApJ*, **731**, 56
- Shevryev, N. N., Zastenker, G. N., Nozdrachev, M. N., et al. 2003, *Adv. Space Res.*, **31**, 1389
- Wu, P., Liu, K., Winske, D., et al. 2010, *J. Geophys. Res.*, **115**, A11105